I&EC research
Industrial & Engineering Chemistry Research

pubs.acs.org/IECR

Article

Pyrolysis Temperature Tunes the Catalytic Properties of CuBTC-Derived Carbon-Embedded Copper Catalysts for Partial Hydrogenation

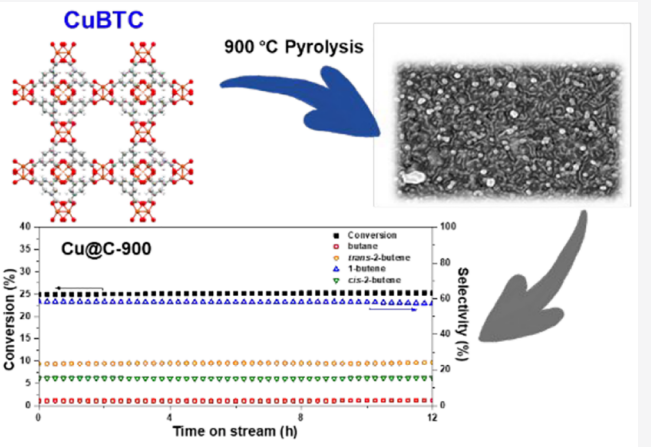
Ahsan Jalal,[‖] Yuxin Zhao,[‖] and Alper Uzun*

Cite This: *Ind. Eng. Chem. Res.* 2022, 61, 2068−2080

Read Online

ACCESS | Metrics & More | Article Recommendations | Supporting Information

ABSTRACT: A family of carbon-embedded copper catalysts was synthesized by pyrolyzing copper benzene-1,3,5-tricarboxylate (Cu-BTC) at various temperatures ranging from 400 to 900 °C. Characterization of catalysts demonstrated that the density of defect sites on the carbon support increases with an increase in the pyrolysis temperature leading to an increase in the electron density on the copper sites. Catalytic performance tests on 1,3-butadiene hydrogenation showed that the performance becomes more stable as the pyrolysis temperature increases above 800 °C such that the catalyst prepared by pyrolysis at 900 °C provided a stable performance for more than 12 h, while the one prepared at 400 °C was deactivating by >25%. Data further demonstrated a strong dependence of the turnover frequencies to the defect site density on the carbonaceous layer. These results present a versatile approach for preparing carbon-embedded copper catalysts with tunable electronic structure and consequent catalytic properties.



Downloaded via KOC UNIV on April 26, 2022 at 20:19:53 (UTC).
See https://pubs.acs.org/sharingguidelines for options on how to legitimately share published articles.

1. INTRODUCTION

The presence of impurities, such as acetylene, 1,3-butadiene, and propyne, in polyolefin feedstocks, is a crucial problem for polymerization units, as these molecules chemisorb on the active sites too strongly and inhibit the activity.[1−3] Thus, their amounts should be reduced below 10 ppm to prevent the catalysts from deactivation.[4] Of interest is the 1,3-butadiene impurity in the feedstock obtained from a C_3/C_4 separator. The partial hydrogenation of 1,3-butadiene increases the purity of these feedstocks without compromising the concentrations of butenes. The catalyst for partial hydrogenation of 1,3-butadiene has two key requirements: (i) high and selective performance for the conversion of 1,3-butadiene into butenes and (ii) a high resistance to deactivation.[4−7]

Industrially, expensive Pd- or Au-based catalysts are employed for the partial hydrogenation of 1,3-butadiene to butenes.[8,9] One of the drawbacks of utilizing these precious metals is their relatively high cost. Moreover, the recycle and lifetime are reduced because of the formation of green oil, which deactivates the catalysts.[1,10] There have been various efforts for making a bimetallic catalyst to get better use of the high selectivity offered by Pd with reduced costs.[11,12] However, each of these catalysts has its own limitations.

Recently, carbon-based supports were found to improve the performance of monometallic Pd catalysts for partial hydrogenation reactions.[13−16] According to these reports, the structure of carbon support greatly influences the electronic environment of Pd and enhances the rate of the hydrogen dissociation. For instance, graphene provides electron rich environment over Pd, which tends to resist coking and favors a high selectivity to partial hydrogenation products.[13] Carbon nitride support was similarly shown to enhance the hydrogen dissociation and Pd activity.[15] It was also noted that acidic sites of carbon nitride tend to isomerize butenes. However, these novel approaches did not help in reducing the cost of the catalysts.

On the other hand, inexpensive metals, such as Cu, Ni, Fe, and Co, can offer economical alternatives to the Pd-based catalysts. These metals provide a significant cost benefit over Pd-based catalysts, as they are several-thousand times cheaper than Pd.[17] However, these inexpensive metals are neither that much active nor selective. In addition to that they tend to deactivate very quickly during the reaction. Recently, it has been noted that the carbon support improves the catalytic

Received: December 2, 2021
Revised: January 13, 2022
Accepted: January 14, 2022
Published: January 31, 2022



© 2022 American Chemical Society

https://doi.org/10.1021/acs.iecr.1c04741
Ind. Eng. Chem. Res. 2022, 61, 2068−2080

performance of these non-noble metals in terms of activity, selectivity, and stability as well.[18−21]

There are numerous methods to prepare carbon-supported catalysts.[22−25] One of the promising approaches is the use of metal organic frameworks (MOFs) as sacrificial templates. In this approach the MOFs are simply pyrolyzed at high temperatures to obtain carbon-embedded metal nanoparticles. Such MOF-derived carbon-supported metal nanoparticles not only offer high metal dispersions at extremely high metal loadings but also possess surface properties that make them appealing for catalysis.[18] For instance, Ni-MOF-74 (metal, Ni; linker, 2,5-dihydroxyterephthalic acid) was pyrolyzed at various temperatures to get a family of highly dispersed carbonaceous nickel nanoparticles. The resulting carbon-embedded nickel catalysts offered a very high selectivity for the selective hydrogenation of olefins.[26] It was reported that Ni nanoparticles were in an electron deficient state and covered by a carbonaceous shell, and this structure was inferred to be the reason for high selectivity for the hydrogenation of 1-octene at 30 °C.[26] In another work, carbon-supported cobalt nanoparticles with varying sizes were obtained by pyrolyzing ZIF-67 (where ZIF stands for zeolitic imidazolate framework with a metal node of Zn and an organic linker of 2-methylimidazole) at different temperatures and tested for the Fischer−Tropsch synthesis. The performance data showed that methane selectivity was higher for Co particle size between 8.4 and 47.8 nm, while improved selectivity for C_2−C_4 hydrocarbons was obtained for particle sizes between 47.8 and 74.8 nm,[19] demonstrating the tunability of the catalytic performance of the MOF-derived carbon-supported metal nanoparticles by the changes in metal nanoparticle size. Moreover, very recently, our group illustrated that pyrolysis of Fe-BTC at 400 °C under flowing N_2 leads to the formation of highly dispersed Fe species covered with a carbonaceous shell. This catalyst was shown to provide a performance superior to some of the best non-noble metal catalysts for producing CO_x-free hydrogen from ammonia decomposition. The characterization data demonstrated that such high and stable performance was associated with the presence of highly dispersed Fe species at a significantly high Fe loading, embedded in a carbonaceous shell, which not only protected the active species against sintering but also made them electron-rich promoting the activity, owing to its high level of graphitization.[27]

Inspired by the success of these studies, here, we focused on copper 1,3,5-benzenetricarboxylate, CuBTC (also known as HKUST-1, with a metal node of copper and an organic linker of benzene-1,3,5-tricarboxylic acid), as a precursor to prepare analogous carbon-embedded Cu nanoparticles. We have chosen this Cu-based MOF as (i) Cu is associated with high selectivity to butenes in 1,3-butadiene hydrogenation, even though it offers a low activity with limited catalytic lifetime,[28−30] and (ii) CuBTC is one of the most studied MOFs with relatively low cost and ease of synthesis.[31] Although there are a few studies using CuBTC as a catalyst precursor,[32−40] there is still a lack of understanding of the relationships between the pyrolysis conditions and the catalytic performance for partial hydrogenation of 1,3-butadiene. Aiming at elucidating these relationships, we synthesized a family of carbon-embedded copper catalysts by pyrolyzing CuBTC at different temperatures, characterized the resulting structures in deep detail, and measured their catalytic performance on partial hydrogenation of 1,3-butadiene. Results demonstrated that the surface properties of carbon and Cu can be tuned by the choice of pyrolysis temperature and these variations in the structure strongly influence the partial hydrogenation performance in terms of activity, selectivity, and stability. These results offer opportunities for the rational design of carbon-embedded copper catalysts by adjusting the pyrolysis temperature according to the required structural characteristics of the active sites toward any target reaction.

2. EXPERIMENTAL METHODS

2.1. Materials and Synthesis. CuBTC (Basolite C300) was purchased from Sigma-Aldrich. Approximately 3 g of CuBTC sandwiched between two layers of quartz wool was placed in a 1/2 in. quartz tube reactor. The loaded samples were then pyrolyzed in a Carbolite split tube furnace (model VST 12/200) in flowing N_2 (150 mL/min, 99.99 vol %, Air Liquide) at 400, 500, 600, 700, 800, and 900 °C for 4 h. The pyrolyzed samples were then cooled down to room temperature in N_2 and passivated at this temperature in 4 vol % O_2 (balance He, 150 mL/min, 99.99 vol %, Air Liquide) for 15 min to make them stable under air exposure. The samples were labeled as "Cu@C-pyrolysis temperature", where Cu@C represents Cu nanoparticles supported/embedded on/in carbon and the "pyrolysis temperature" corresponds to 400, 500, 600, 700, 800, and 900 °C. For instance, Cu@C-700 stands for a carbon-embedded copper sample synthesized by pyrolyzing CuBTC at 700 °C. For benchmark measurements an activated carbon (AC) (DESOREX K33) sample was also used. This sample was kindly supplied by Mikropor.

2.2. Thermogravimetric Analysis (TGA). TGA of the pristine CuBTC was performed on a TA Instruments TGA Q500 model instrument under nitrogen flow (60 mL/min for sample, 40 mL/min for balance purge). Approximately 15 mg of CuBTC was placed in a platinum pan. The temperature was first raised to 110 °C at a ramp rate of 20 °C/min. Then it was held constant at 110 °C for 2 h. Later, the temperature was raised to 950 °C at a ramp rate of 5 °C/min to complete the measurement. T'_{onset} was determined by extrapolation from the derivative of the thermogravimetry curves, as before.[41]

2.3. Temperature-Programmed Reduction (TPR). TPR measurements on the pyrolyzed samples were carried out on a Micromeritics AutoChem II 2920 automated catalyst characterization system coupled with an MKS Cirrus II mass spectrometer. Samples were first heated to 100 °C in He flow (at 30 mL/min) for 30 min. Then, they were heated at a rate of 3 °C/min up to 700 °C (or to their corresponding pyrolysis temperature if it is lower than 700 °C) in flowing 10 vol % H_2−Ar (30 mL/min, Air Liquide). The effluent gas stream was monitored continuously using an online thermal conductivity detector (TCD).

2.4. Scanning Electron Microscopy (SEM). A Zeiss Ultra Plus (FEG-SEM) scanning electron microscope with a secondary electron (SE) detector was utilized to obtain the SEM images. Samples were placed on a carbon tape to prevent from the charging effect. The images were collected at a magnification of (1−100)k× with an accelerating voltage (EHT) of 3 kV and at a working distance in the range of 4.5−4.7 mm.

2.5. Microanalysis by Transmission Electron Microcopy (TEM) and Scanning Transmission Electron Microcopy (STEM). The microanalysis was carried out at 200 kV using a Hitachi Hi-tech HF5000 TEM/STEM system with a third order aberration corrector and a cold FEG electron source. The microscope was equipped with an Oxford 100

https://doi.org/10.1021/acs.iecr.1c04741
Ind. Eng. Chem. Res. 2022, 61, 2068−2080

mm^2 silicon drift twin energy-dispersive spectrometer, providing a solid angle of 1.7 sr. It was also equipped with a secondary electron detector allowing simultaneous imaging in scanning electron (SE), bright field (BF), and dark field (DF) modes at 200 kV. The sample powders were loaded into a holey carbon (Ted Pella) grid prior to installing the grid into the sample holder.

2.6. X-ray Fluorescence (XRF) Spectroscopy. A Bruker S8 Tiger XRF spectrometer in standardless mode under He gas atmosphere with an 18 mm mask was used for the XRF analyses. Powder samples were placed into an XRF sample cup (Chemplex Industries Inc., catalog no. 1430) with a thin film support (Prolene film with 4 μm thickness, Chemplex Industries, Inc., catalog no. 426). Typical impurities arising from this film were Ca, P, Fe, Zn, Cu, Zr, Ti, and Al at ppm levels. The loose powder method in addition to the "best analysis" options was used for analysis. The SpectraPlus Eval2 V2.2.454 software was employed for the data analysis.

2.7. X-ray Diffraction (XRD). XRD measurements were performed with a Bruker D8 Discover X-ray diffraction system equipped with a Cu Kα1 radiation source with a wavelength of 1.54 Å. The power rating of the X-ray generator was set to 40 kV and 40 mA. A Vantec-1 detector was used with a slit size of 1 mm. The measurements were performed in the range of 2θ values of 5−50° with a step size of 0.0126°. Approximately 5 mg of sample was loaded on a double-sided tape stick on a glass. Then, it was placed on a sample holder by a plasticine gum. The signal was subjected to subtraction of background signal generated by the tape. ICDD PDF-4 2014 database was used for phase identification. Average particle size was determined by applying the Scherrer equation.[42]

2.8. Raman Spectroscopy. Raman spectroscopy measurements of the samples were performed with a Renishaw inVia Raman microscope equipped with a 532 nm/100 mW laser excitation source. Calibration of the Raman spectrum was done by using a silicon wafer at 520 cm^{-1}. Laser intensity was kept at 10% of the total intensity to avoid burning of the sample. The spectrum was collected for 1 s at a rate of 60 accumulations per spectrum.

2.9. Brunauer, Emmett, and Teller (BET) and Barrett, Joyner, and Halenda (BJH) Analyses. For the BET surface area analysis, a Micromeritics ASAP 2020 physisorption analyzer was used. Approximately 150 mg of the samples was activated at 125 °C under vacuum. The samples were cooled by using liquid nitrogen. Helium was employed for free-space measurements. Isotherms of nitrogen adsorption were obtained at a pressure range from 10^{-6} to 1 bar. To estimate the surface area of the samples, the BET equation was applied for pressures between 0.08 and 0.25 bar. Pore volumes of the samples were obtained from the N_2 adsorption isotherm at −196 °C using the BJH method.

2.10. N_2O Chemisorption and H_2 Pulse Reduction Method. The amounts of the corresponding exposed Cu species on the reduced catalysts were determined on a Micromeritics AutoChem II 2920 apparatus equipped with a TCD by N_2O chemisorption followed by H_2 pulse reduction based on [$2Cu(s) + N_2O \rightarrow Cu_2O(s) + N_2$], where Cu(s) represents a surface Cu atom. The measurement steps are described as follows: (i) Fresh catalysts after the water removal step were reduced in flowing 10 vol % H_2 in balance Ar at 175 °C for 1 h to remove the oxide layer formed during the passivation treatment, and (ii) the reduced Cu sites on the surface were oxidized to Cu^+ by N_2O; (iii) the surface Cu_2O was reduced to Cu^0 by dosing the catalyst with H_2, and the amount of H_2 consumption was denoted as X. Pulse dosing was repeated at an interval of 3 min until the detected TCD peaks for the latest three or more pulses were constant in area. The corresponding exposed Cu species amounts in each catalyst were equal to $2X$.[43]

2.11. Catalytic Activity Testing. Catalytic activities of the samples were measured in a 1/2 in. stainless steel tubular once-through flow reactor. Temperature was controlled by a PC-operated Thermcraft three-zone resistively heated furnace (model no. XST-3-0-18-3V). Alicat MC series gas mass flow controllers were used to control the gas flow rates. Pristine CuBTC was activated at 150 °C under He flow for obtaining the benchmark data. The passivated pyrolyzed samples were mixed with SiO_2 (calcined at 500 °C and tested prior to confirm the catalytic inertness) at a ratio of 1:5 wt/wt (catalyst/SiO_2) and reactivated in H_2 flow at 175 °C and ambient pressure for 1 h prior to use. The total gas flow rate was adjusted to 10 mL/min. The reaction was carried out at different temperatures from 60 to 300 °C under ambient pressure with a feed H_2/1,3-butadiene molar ratio of 1:1 (H_2, Air Liquide, 99.99 vol %; 1,3-butadiene, Linde, 99.6 vol %). An online Agilent GC 7890A equipped with a GS-alumina column (50 m × 530 μm) and a flame ionization detector (FID) was employed for the quantification of the concentration of reactants and products. The column temperature was kept constant at 130 °C, and He (carrier) flow rate was 6.5 cm^3/s during the measurements. For comparison, a Cu@C-900&AC catalyst mixture was prepared by physically mixing Cu@C-900 with AC at a ratio of 1:1 wt/wt (catalyst/AC). Reproducibility of the measurements was checked by testing different batches of samples under identical conditions. The results demonstrated that both the conversion and selectivity values were consistent within less than 5% on each catalyst considered.

3. RESULTS AND DISCUSSION

Figure S1 presents the TGA results of the as-received CuBTC along with its structure. The data showed a weak peak at 210 °C associated mainly with the dehydration of CuBTC.[44] According to the study of Al-Janabi et al., the BTC ligand decomposes with the release of oxygen, and the oxygen reacts with Cu to form Cu_2O at approximately 280 °C. Later these newly formed Cu_2O species undergo further transformation to form the mixture phases of Cu_2O and Cu because of the simultaneous release of reducing agents, such as CO, CH_4, and H_2, during pyrolysis at approximately 350 °C.[26,44] Consistently, our data showed that the major decomposition step, including the loss of approximately 40 wt % of the initial mass, started at a T'_{onset} of 335 °C, as in the case of our earlier reports on the utilization of CuBTC for gas separation applications.[41,45] Therefore, we decided on a set of pyrolysis temperatures to obtain a family of supported copper catalysts with different surface characteristics as 400, 500, 600, 700, and 900 °C, ensuring that the framework collapsed to form Cu nanoparticles.

The samples prepared by pyrolyzing the as-received CuBTC at these set temperatures were characterized in deep detail to identify the differences in their structural characteristics and the dependency of these differences on the pyrolysis temperature. For this purpose, all the samples were passivated at room temperature in 4 vol % O_2 before their *ex situ* characterization to prevent copper nanoparticles from being oxidized by air. Table 1 summarizes the BET and BJH analysis

https://doi.org/10.1021/acs.iecr.1c04741
Ind. Eng. Chem. Res. 2022, 61, 2068−2080

Table 1. Physical Properties of CuBTC and Pyrolyzed Samples

sample	Cu crystallite size (nm)[a]	Cu (wt %)[b]	BET (m^2/g)[c]	pore volume (cm^3/g)[d]	D_P (nm)[d]	exposed Cu amount ($\times10^{-4}$ mol/g)[e]	available Cu (mol %)[f]
CuBTC	nd[g]	58.1	1324	0.83	2.7	nd[g]	n.d.
Cu@C-400	23.9	88.7	46.7	0.03	5.1	1.02 ± 0.11	17.5
Cu@C-500	23.8	88.9	187.3	0.07	4.1	1.14 ± 0.02	19.4
Cu@C-600	25.5	89.3	174.2	0.03	3.9	1.10 ± 0.03	19.9
Cu@C-700	26.4	89.7	196.7	0.06	4.9	1.13 ± 0.01	21.1
Cu@C-800	24.7	90.0	183.4	0.03	4.2	1.10 ± 0.03	19.2
Cu@C-900	23.6	90.3	174.2	0.04	5.3	1.16 ± 0.03	19.3

[a]Measured by XRD and determined by the Scherrer equation. [b]Determined by XRF. [c]Determined by the BET method. [d]Determined by the BJH method. [e]Calculated by N_2O chemisorption and the H_2 pulse reduction method. [f]The available copper ratio (mol %) was calculated as the ratio of the amount of exposed copper amount determined by the pulse chemisorption measurements and the theoretical surface copper amount determined by the corresponding average copper nanoparticle size. [g]nd: not detected.

results. Accordingly, the surface areas of the pyrolyzed samples, except for the one prepared at 400 °C, were nearly the same within the error range of our measurements. Data showed a decrease from a value of 1300 m^2/g on the pristine CuBTC to approximately 140 m^2/g on all the pyrolyzed samples except for Cu@C-400, which has a much lower surface area of approximately 50 m^2/g. This difference on Cu@C-400 could originate from the fact that the pyrolysis temperature of 400 °C used to prepare this catalyst was below the temperature required to create porous carbon.[18] These results suggest that the framework of the CuBTC collapsed upon the heat treatment in N_2 flow, as expected, and the specific surface area of the porous carbon-coated catalyst is not affected by the pyrolysis temperature.

Figure 1 compares the XRD results of the pyrolyzed samples with that of the pristine CuBTC. Accordingly, the pyrolyzed samples consistently lack any features belonging to the pristine CuBTC and present a distinct feature at 43.4°, indicating the presence of the metallic Cu nanoparticle. In line with Al-Janabi et al., the Cu@C-400 sample showed a weak characteristic diffraction feature of Cu_2O at 37.3°, probably generated because of the oxygen release from BTC ligand during pyrolysis at a relatively low temperature (400 °C).[44] However, as the pyrolysis temperature increased, none of the other samples showed the characteristic diffraction feature of Cu_2O, indicating that the trace amount of Cu_2O species was wholly reduced to Cu under higher pyrolysis temperature conditions.

Furthermore, applying the Scherrer equation on the band at 43.4° indicates that the average Cu(111) crystallite sizes of the

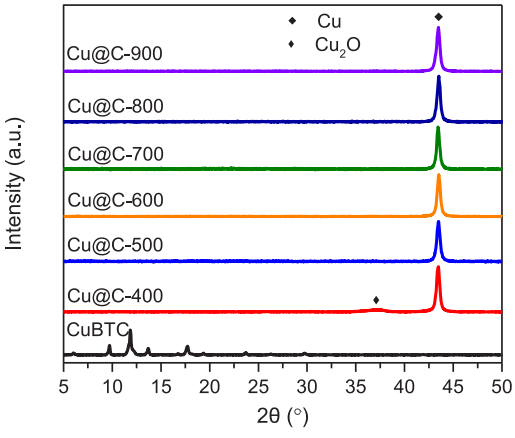


Figure 1. XRD of CuBTC and the samples prepared by pyrolyzing CuBTC at different temperatures.

copper nanoparticles were almost the same at 25.5 ± 1.2 nm on each sample (Table 1). Thus, we inferred that the pyrolysis of CuBTC even at 400 °C leads to the formation of copper nanoparticles embedded in carbon, already large enough that their sizes do not get any larger with a further increase in the pyrolysis temperature, as was the case in Fe nanoparticles derived from Fe-BTC.[27] Besides, the XRF data summarized in Table 1 showed that the corresponding Cu loading (wt %) of the samples increases from 58 wt % on the pristine CuBTC to approximately 90 wt % on the pyrolyzed samples. These results confirm our inference that the size and amount of the copper nanoparticles formed during the pyrolysis of CuBTC at different temperatures were almost independent of the pyrolysis temperature.

The electron microscopy analysis was further performed to analyze the structure of the catalyst visually. Figure S2 demonstrates the representative SEM images collected on each of the pyrolyzed samples along with that of the pristine CuBTC. The images showed that the morphology of the pyrolyzed samples and the pristine CuBTC remains similar at a macro level irrespective of the pyrolysis temperature. These similarities in the external structures agree well with an earlier report by Zhao et al., reporting that a CuBTC-derived catalyst prepared by pyrolysis at 350 °C showed a similar octahedral structure (externally) with the pristine CuBTC. Their high-resolution TEM images indicated that the pyrolysis led to the formation of copper nanoparticles encapsulated by octahedral carbon, preventing their further aggregation from forming large Cu nanoparticles. They noted that a small amount of Cu nanoparticles was accumulated at the external surface.[35] They also reported that the agglomeration process was limited with the pyrolysis conditions; when the treatment was done under a reducing atmosphere, the Cu nanoparticles severely agglomerated. Similarly, our SEM images presented in Figure S2 demonstrated that the external structure of the particles present in the pyrolyzed CuBTC samples is similar to those of the pristine CuBTC. However, the images obtained at higher magnifications demonstrated the presence of spherical Cu nanoparticles on the external surface of these particles. We note that these SEM images at relatively low magnification did not provide any evidence of the encapsulation of Cu particles by carbon (Figure S2).

However, microanalysis of the representative samples, Cu@C-400 and Cu@C-900, by obtaining images simultaneously in SE, BF, and DF modes by using an aberration-corrected transmission electron microscope illustrated clearly that the Cu nanoparticles of 25−40 nm were covered with a carbonaceous

https://doi.org/10.1021/acs.iecr.1c04741
Ind. Eng. Chem. Res. 2022, 61, 2068−2080

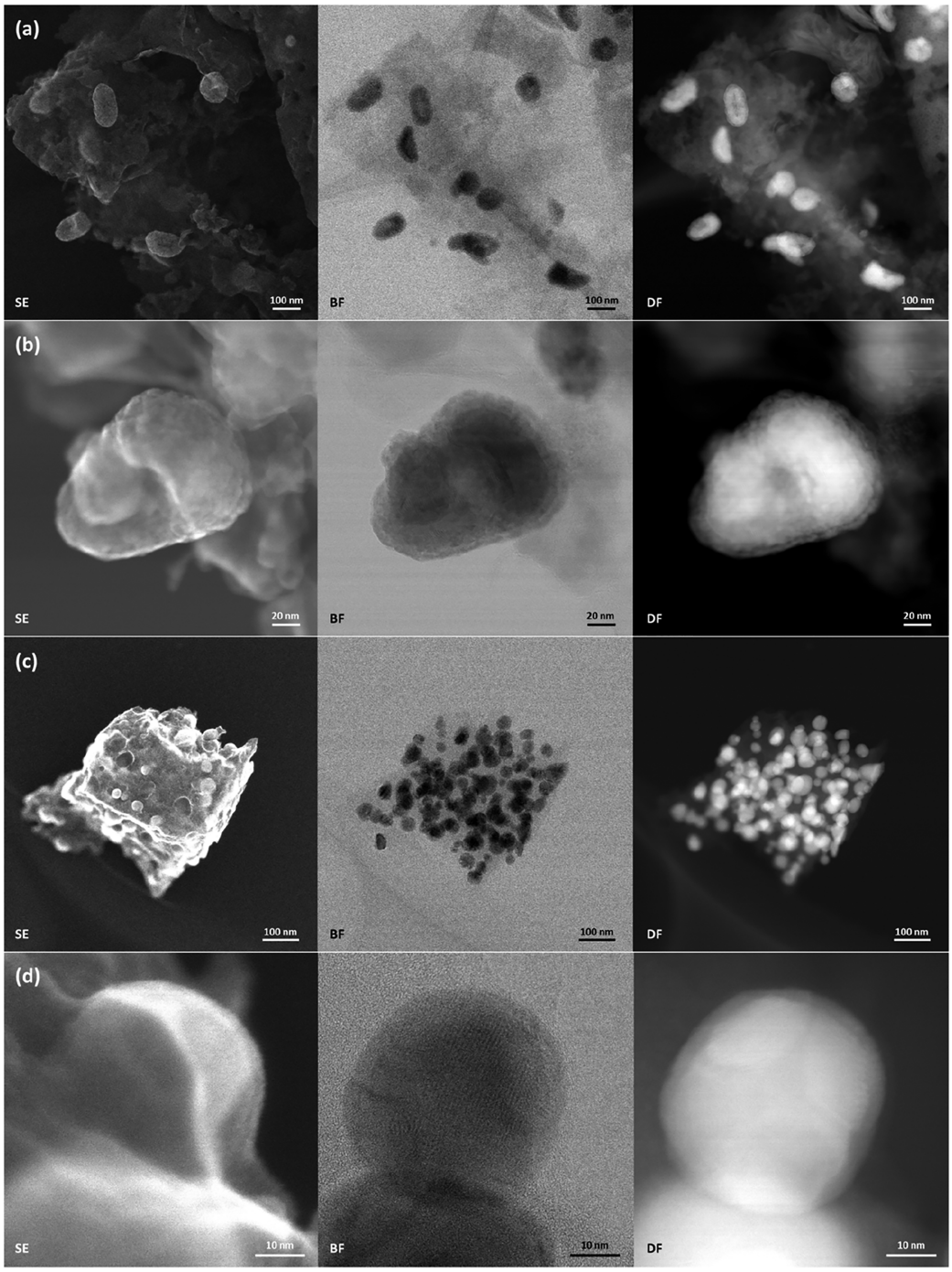


Figure 2. Microanalysis of representative samples, Cu@C-400 ((a) at 20K× and (b) at 100K×) and Cu@C-900 ((c) at 26K× and (d) 360K×). Images were obtained simultaneously in SE, BF, and DF modes. Images obtained at a higher magnification indicate the presence of copper agglomerates made up of small nanoparticles embedded/covered in/with amorphous carbon.

shell formed by the collapse of the framework (Figure 2). For instance, Figure 2a and Figure 2b show that pyrolysis at 400 °C led to the formation of porous copper agglomerates with an approximate size of 100−150 nm. Images obtained at a higher magnification indicated that these agglomerates are made up of small copper nanoparticles embedded/covered in/with amorphous carbon. Moreover, the images obtained on Cu@C-900 (Figure 2c and Figure 2d) illustrated that pyrolysis at 900 °C resulted in the formation of similar carbon-embedded copper agglomerates but with less porous structure and more complete formation of copper nanoparticles. As in the case of Cu@C-400, these nanoparticles were covered with a porous carbonaceous shell. Because of the presence of this carbon shell, it was not possible to resolve the smaller copper nanoparticles completely. Thus, we preferred not to attempt estimating the average copper nanoparticle size from these electron microscopy images. However, as discussed above, these images illustrate clearly that the copper nanoparticles form highly porous agglomerates with carbon upon the pyrolysis of CuBTC. Therefore, it is more critical to analyze

https://doi.org/10.1021/acs.iecr.1c04741
Ind. Eng. Chem. Res. 2022, 61, 2068−2080

the properties of porous carbon, its interaction with the copper nanoparticles, and the number of accessible active sites in each catalyst.

As mentioned above, copper nanoparticles generated by pyrolysis were embedded in porous carbon. However, the porous carbon cannot play a role as an active site alone in most catalytic reactions. Herein, we further evaluated the changes in the exposed copper amounts in the activated samples by N_2O chemisorption followed by H_2 pulse reduction measurements. Before the measurement, the H_2-TPR method was used to determine the reducing temperature of the oxide layer formed by passivation. As shown in Figure S3, H_2-TPR results demonstrated that the copper oxide layer could be reduced easily at a relatively low temperature of approximately 160 °C. Thus, we set the temperature for the activation of our catalysts to 175 °C, slightly higher than 160 °C, to make sure the oxide layer over the copper nanoparticles could be successfully removed. The corresponding exposed copper amounts in the activated catalysts measured by chemisorption following their reduction treatments are listed in Table 1. The results clearly showed that the exposed copper amounts of all the six catalysts were approximately equal to 1.13×10^{-4} mol/g (Figure S4) within $\pm 3 \times 10^{-6}$ mol/g as in the case with the specific surface areas. Here, we note that the amount of surface copper species is not used to determine the dispersion of copper particles or the size of copper particles. Unlike the supported copper-based catalyst, the surface copper species here represent the copper species that can participate in the subsequent reactions under the porous carbon coating. Therefore, it is not suitable to use it for the analysis of the average copper nanoparticle size but it is more suitable to call them the exposed copper species in this catalytic system. Meanwhile, under the premise that the porous carbon layer is uniformly distributed, the exposed copper species that is not affected by the pyrolysis temperature also indicated that the composition of the surrounding porous carbon structure can be the dominant factor that affects the catalytic properties of the exposed copper species.

Next, the Raman spectra were measured to investigate the porous carbon structures. Data presented in Figure 3 demonstrate the presence of the expected peaks at 1353 and 1584 cm^{-1} corresponding to the D-band, associated with the vibrations of electron-deficient sp^3 carbon atoms of defects or

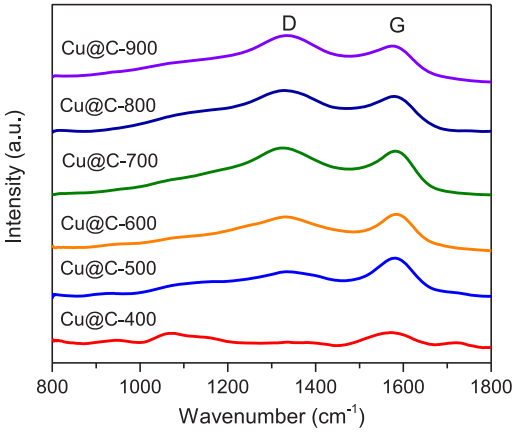


Figure 3. Raman spectra of pyrolyzed CuBTC samples at different temperatures. Peaks at 1353 and 1584 cm^{-1} correspond to the D-band and G-band showing defects and graphitic nature of carbon, respectively.

with the breathing mode of six-atom rings, and the G-band,[46,47] associated with the vibration of electron-rich sp^2 carbon atoms in a graphitic 2D hexagonal lattice, respectively. Besides, between the two types of carbon species, in the area between 1400 and 1550 cm^{-1}, there is a valley area "V" contributed by small amorphous carbon.[48] Here, we focused on the ratio of the intensities of these bands, I_D/I_G ratio, to quantify the degree of disorder in the corresponding carbonaceous shells covering the copper nanoparticles by the pyrolysis of CuBTC at different temperatures. Accordingly, an increase in the I_D/I_G ratio represents an increase in the degree of disorder or the surface density of defects. We note that it might also be associated with an increase in the degree of aromatization. However, as demonstrated below, the XPS data rule out this possibility.[49−51]

Figure 4a illustrates that the I_D/I_G ratio presents a gradual increase from 0.5 to 1.3 with respect to pyrolysis temperature with an R^2 value of 0.97. This increasing trend indicates that the defect concentration increases with an increase in pyrolysis temperature. Meanwhile, one can observe that the ratio I_D/I_G has a strong linear correlation with I_V/I_D; as I_D/I_G increases, I_V/I_D decreases significantly (Figure 4b). This relationship reveals that the formation of the D structure may be related to the condensation of small amorphous structures during pyrolysis.[48] On the basis of these results, it can be inferred that the presence of Cu-based nanoparticles at significantly high amounts can cause structural distortions on the carbon support, increasing the defect amounts in the carbon matrix leading to an increase in the D bands.[52] One can argue that on other carbon-based materials the number of graphitic features was expected to increase with an increase in pyrolysis temperature (i.e., a low I_D/I_G ratio).[53,54] However, data presented here on the pyrolyzed CuBTC samples present an opposite trend, which is consistent with the findings reported by Weng et al., where Cu-BTC samples obtained by annealing in Ar in a temperature range of 400−900 °C provided a similar trend such that an increase in pyrolysis temperature led to a decrease in graphitic structure.[52] Our recent results on the carbon-embedded Fe catalysts prepared by the pyrolysis of Fe-BTC also demonstrated a similar trend.[27] Therefore, it can be considered that the tendency of porous carbon structure change in the pyrolysis process of CuBTC is reasonable.

Consistent with the Raman results, C 1s XP spectra (Figure 5a) of the samples were characterized by four features located at approximately 284.6, 285.2, 286.3, and 289.4 eV, corresponding to $sp^2_{C=C}$, sp^3_{C-C} defect, C−O, and C═O, respectively. Figure 5b indicates that the increase in the ratio of I_D/I_G was accompanied by an increase in the ratio of $sp^3_{C-C}/sp^2_{C=C}$. Thus, we confirm that the increase in the ratio of I_D/I_G is mostly associated with an increase in the sp^3_{C-C} defect rather than an increase in the degree of aromatization.

To further investigate the effect of porous carbon coating on the electronic environment of the interface of these newly formed copper nanoparticles, we performed XPS measurements (Figure 6a and Figure S5). Figure S5 demonstrates the XP spectra of the samples from 925 to 965 eV corresponding to Cu 2p core levels. Upon deconvolution of the Cu $2p_{3/2}$ spectra of the pyrolyzed Cu@C-400, the spectra revealed two types of Cu species. The first one appeared between 932 and 934 eV, corresponding to the surface of copper nanoparticle in the metallic form.[32,55] The other one appearing at 934.7 eV was very weak, associated with the oxides of Cu.[34,56] We also note that the data do not present any satellite peaks, indicating

https://doi.org/10.1021/acs.iecr.1c04741
Ind. Eng. Chem. Res. 2022, 61, 2068−2080

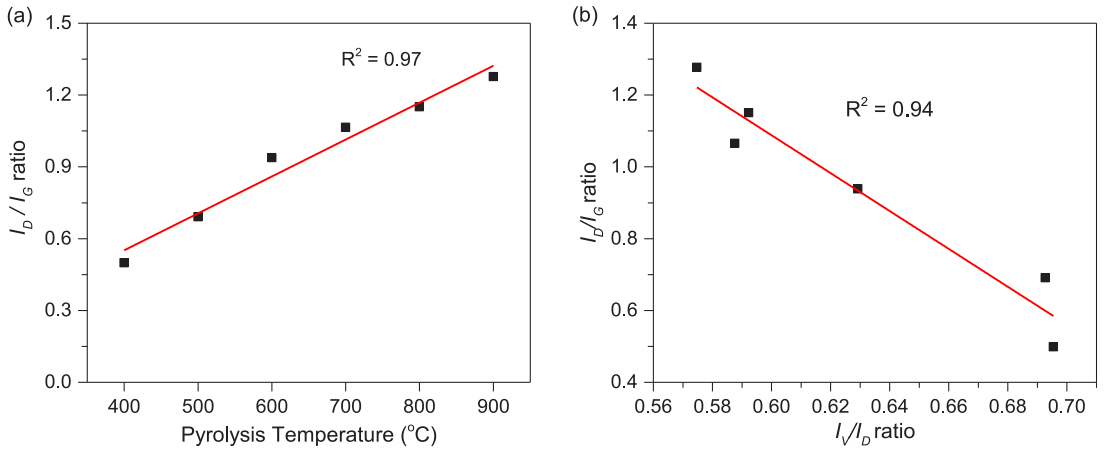


Figure 4. (a) Variation of I_D/I_G ratio with the pyrolysis temperature; (b) I_D/I_G ratio as a function of I_V/I_D ratio.

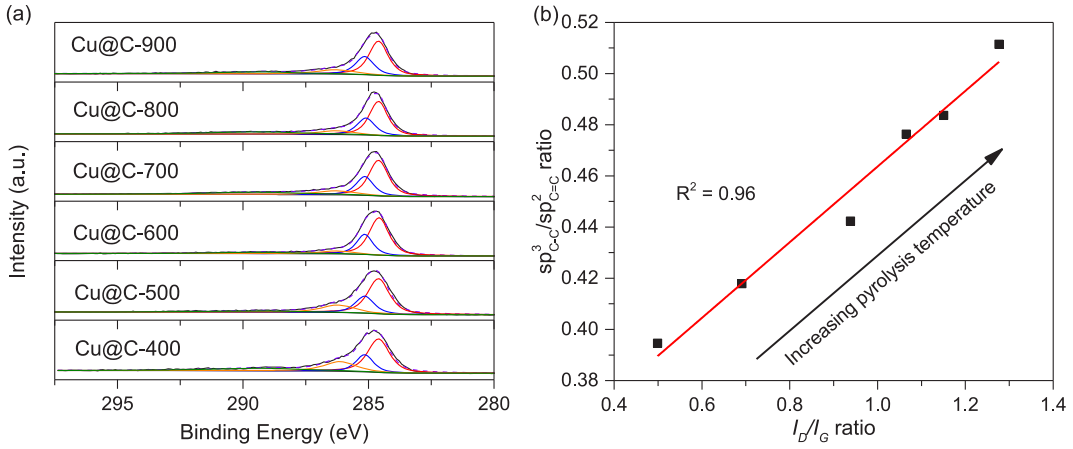


Figure 5. (a) XP spectra of C 1s for the samples prepared by pyrolyzing CuBTC at different temperatures; (b) variation of $sp^3_{C-C}/sp^2_{C=C}$ ratio as a function of I_D/I_G ratio.

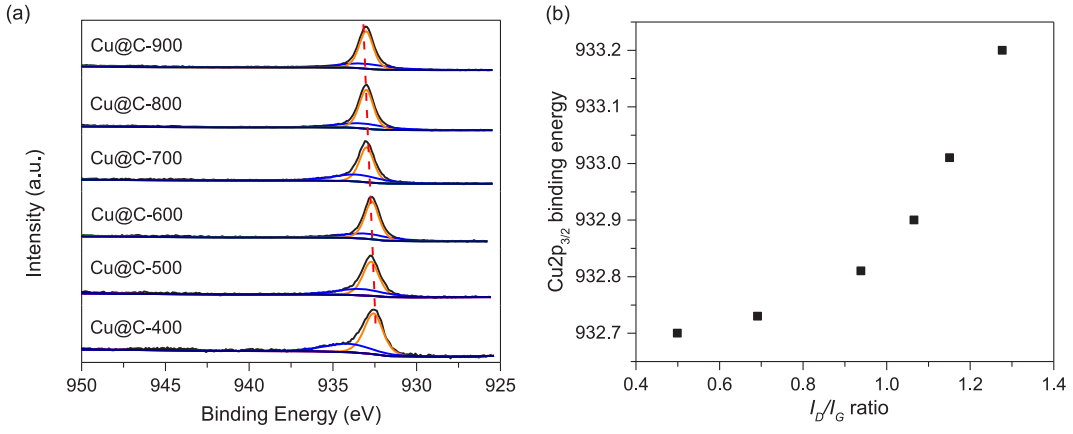


Figure 6. (a) XP spectra of Cu $2p_{3/2}$ for the samples prepared by pyrolyzing it at different temperatures; (b) Cu $2p_{3/2}$ binding energy of the copper sites as a function of I_D/I_G ratio.

the high purity of the copper crystallites formed during the pyrolysis of CuBTC.[57] Consistent with the XRD results, these XPS results indicated the presence of copper nanoparticles as the dominant species on the surface, along with some oxides of Cu, which might be generated from the passivation process. The XPS data further indicated that the position of the copper-binding energy on different samples shifts with a change in the pyrolysis temperature, as shown in Figure 6a. Accordingly, the metallic Cu peak shifts to a higher energy as the pyrolysis temperature increases above 500 °C, from 932.7 eV on Cu@C-400 to 933.2 eV on Cu@C-900. This blue-shift in binding energy indicates a decrease in the electron density on the copper sites with an increase in pyrolysis temperature, as an increasing trend in the corresponding binding energy of metallic Cu $2p_{3/2}$ with an increase in the I_D/I_G ratio (Figure 6b). This result is consistent with an earlier report showing

https://doi.org/10.1021/acs.iecr.1c04741
Ind. Eng. Chem. Res. 2022, 61, 2068−2080

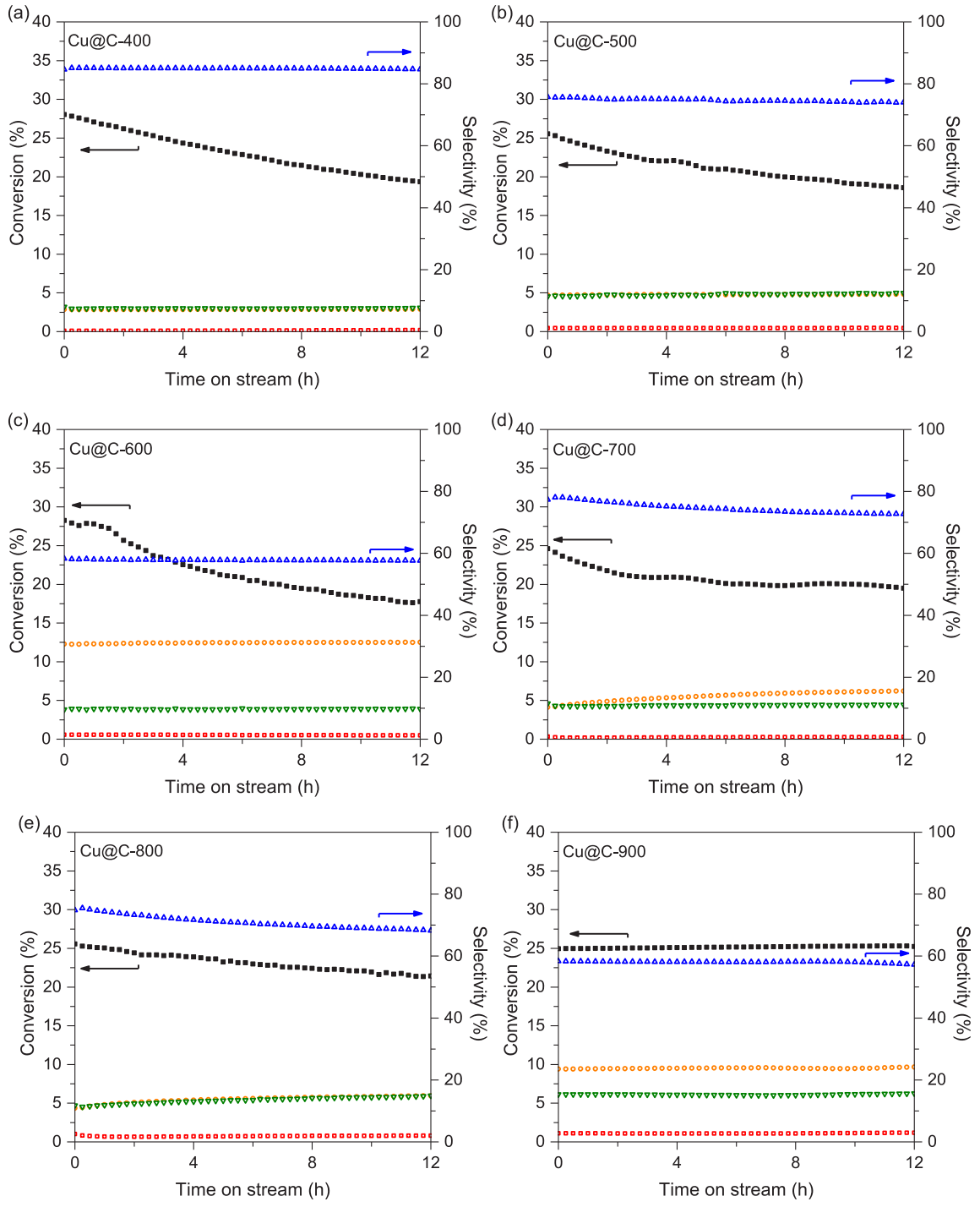


Figure 7. Variation of 1,3-butadiene conversion and product selectivities with TOS for partial hydrogenation of 1,3-butadiene at 130 °C and 1 bar using a feed mixture having a 1,3-butadiene to hydrogen ratio of 1:1 using catalysts prepared by the pyrolysis of CuBTC at different temperatures: (a) Cu@C-400, (b) Cu@C-500, (c) Cu@C-600, (d) Cu@C-700, (e) Cu@C-800 °C, and (f) Cu@C-900 °C. GHSV was varied within the range of 6000−2800 mL of 1,3-BD × g_{cat}^{-1} × h^{-1} to reach approximately the same initial conversion for each catalyst. Closed symbol: 1,3-butadiene conversion (solid black box). Open symbols: selectivity for butane (red box); 1-butene (blue up-triangle); *cis*-2-butene (black down-triangle); *trans*-2-butene (red circle).

that electron-deficient nickel particles with carbon shell were derived from Ni-MOF-74 upon pyrolysis at 300 °C.[26] Thus, we infer that the changes in the pyrolysis temperature can tune the electronic properties of the copper sites.

To investigate the effect of pyrolysis temperature on the catalytic properties, we performed the performance tests at 130 °C and 1 bar using a feed mixture having a 1,3-butadiene to hydrogen ratio of 1:1. As a comparison, we also performed identical tests on the pristine CuBTC as well, and the results indicated that the pristine CuBTC did not have any activity for hydrogenation under these conditions. Different from the low selectivity of palladium-based catalysts under high conversions, the selectivity of copper-based catalysts can usually be maintained at a very high level. Correspondingly, the stability

https://doi.org/10.1021/acs.iecr.1c04741
Ind. Eng. Chem. Res. 2022, 61, 2068−2080

of copper-based catalysts under relatively mild conditions can better demonstrate the catalyst's real performance. Therefore, the 1,3-butadiene conversion in the evaluation of the catalysts lifetime was controlled at a relatively low level (<30%). Figure 7 demonstrates the variation of 1,3-butadiene conversion and the selectivity of individual products with time-on-stream (TOS) for each catalyst listed in Table 1. Accordingly, each catalyst provides a significantly high and constant partial hydrogenation selectivity of above 98%. While the total butene selectivity was almost complete on Cu@C-400 (Figure 7a), the selectivity decreases slightly to 98.5 ± 0.7% with an increase in pyrolysis temperature from 400 to 900 °C. Figure 7 shows that even though the total butene selectivity of the samples was almost the same (approaching complete selectivity for partial hydrogenation) for each sample, the individual butene selectivities vary with the pyrolysis temperature, the most significant variation being on the 1-butene selectivity. Data showed that the 1-butene selectivity decreases from approximately 85 to 57% as the pyrolysis temperature increases from 400 to 900 °C, and this increase was mostly associated with an increase in the selectivity of *trans*-2-butene. This decrease might be associated with the electron deficient character of the Cu nanoparticles of the Cu@C-900 caused by the presence of a higher density of defect sites. Because of this electron deficient character, carbon support might be participating in the reaction network to boost the isomerization reaction of 1-butene to 2-butenes. Huang et al. reported that on supported Pd, the acidic nature of support, g-C_3N_4, results in different distribution of individual butenes as compared to graphene, lacking any acidic character.[15] Moreover, Nieminen et al. reported that the electron deficient Cu acts as an acid. They noticed that the electron deficient copper species promote the protonation of carbon C1 giving intermediates, favoring the skeletal isomerization of 1-butene to isobutene.[58] This inference is consistent with an earlier report, where zeolite-X-supported Cu was found to be more active than zeolite-X for the isomerization of 1-butene to 2-butenes.[59] We also noticed that *trans*- to *cis*-2-butene ratio remains at approximately 1.0 except for the samples prepared by pyrolysis at 600 and 900 °C. Here, we note that 85% selectivity for 1-butene (with an almost complete selectivity for partial hydrogenation) obtained on Cu@C-400 is notably high and presents a broad potential for industrial applications needing 1-butene as the raw material.[13] On the basis of these results, we inferred that the structural (mostly electronic) variations on the active sites induced by the changes in the pyrolysis temperature influence the reaction network leading to significant changes in the individual product distribution.[60] For comparison, the catalytic performance of an AC sample having an I_D/I_G ratio of 0.95 was also evaluated. Data presented in Figure S6 indicate that the hydrogenation activity of the AC at the same space velocity is less than 2%. Thus, considering our samples prepared by pyrolyzing CuBTC contain less than 10 wt % carbon, we infer that the contribution of the carbon content of the catalysts to the overall 1,3-butadiene conversion should be negligible (less than 0.2%). Here, we also note that the defect sites on the carbonaceous layer might also play a role in providing a secondary reaction pathway involving isomerization of the partial hydrogenation products, possibly affecting the individual butene selectivity, as noted above. To rule out this possibility, we performed an additional experiment by physically mixing Cu@C-900 with an AC sample and measured the activity. The data (presented in Figure S7) indicated that the addition of AC does not change the product selectivities. Thus, we infer that the influence of the carbonaceous layer on the secondary reactions is negligible.

Here, we note that, in Figure 7, we adjusted the space velocities on each sample to be able to get a comparable initial 1,3-butadiene conversion to determine the differences in their TOS behavior. This difference in space velocities suggests variations in the 1,3-butadiene conversion rates on different catalysts. Thus, next, we compared the variation of these rates in mol of 1,3-butadiene converted × (mol of all Cu × s)$^{-1}$ in Figure 8. Comparison showed that Cu@C-400 provides the highest initial 1,3-butadiene conversion rate. Figure 8 further demonstrates that the catalysts show deactivation within 12 h except for Cu@C-900, which maintains its initial activity (and almost complete partial hydrogenation selectivity) for at least 12 h. Because Cu@C-900 provides a stable performance, we evaluated its performance at a wider space velocity range to investigate the product selectivities at especially high conversions, providing a feed composition mimicking those of the realistic industrial feeds with very high olefin concentrations. As shown in Figure 9, the total partial hydrogenation selectivity on Cu@C-900 remains above 97% even at a 1,3-butadiene conversion of 98%.

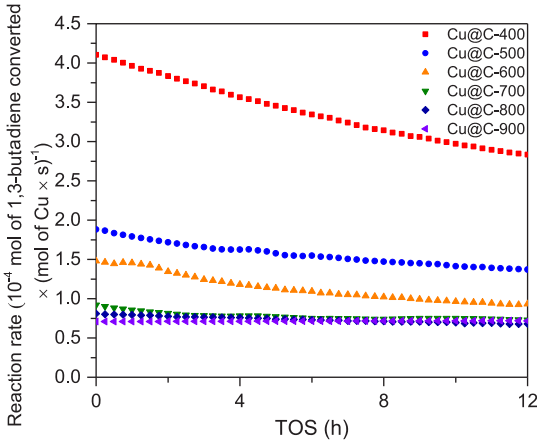


Figure 8. Variation of 1,3-butadiene hydrogenation with TOS on each catalyst at 130 °C and 1 bar using a feed mixture having a 1,3-butadiene to hydrogen ratio of 1:1.

To understand the reasons responsible for the differences in hydrogenation activity, we also evaluated the variation of initial turnover frequency (TOF_i, in mol of 1,3-butadiene converted/(mol of exposed Cu × s) values calculated on the basis of the amount of exposed copper species with the corresponding Cu $2p_{3/2}$ peak positions and the I_D/I_G ratios as shown in Figure 10. The data presented in Figure 10 demonstrated a strong dependency of the TOF_i values on the corresponding I_D/I_G ratio of the carbon support. Accordingly, the TOF_i decreases significantly with an increase in pyrolysis temperature (characterized by an increase in both Cu $2p_{3/2}$ peak position and the I_D/I_G ratio) such that the TOF_i of Cu@C-400 was approximately one order of magnitude higher than that of Cu@C-900. Thus, we infer that as the density of electron deficient defect sites increases on the support with an increase in the pyrolysis temperature, the catalytic activity decreases. However, data also suggested that even though the changes in carbon support lead to a lowering in TOF_i, the catalysts become much more stable with this structural change. On the

https://doi.org/10.1021/acs.iecr.1c04741
Ind. Eng. Chem. Res. 2022, 61, 2068−2080

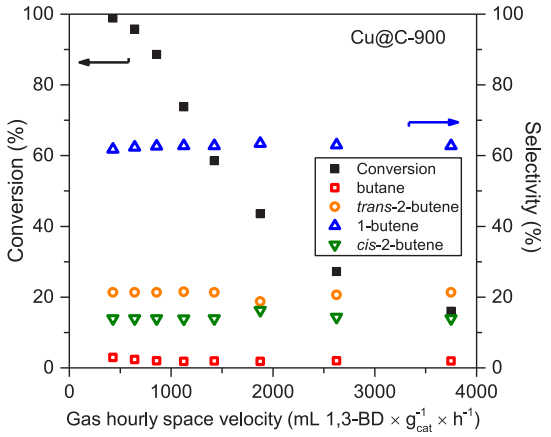


Figure 9. 1,3-Butadiene conversion and product selectivity as a function of GHSV (in mL of 1,3-BD × g_{cat}^{-1} × h^{-1}) for Cu@Cu-900. Reaction conditions: 130 °C, 1 bar using a feed mixture having a 1,3-butadiene to hydrogen ratio of 1:1.

basis of these differences in performance, we suggest that the high rate of deactivation on the samples with high TOF_i values might originate from the enhanced generation rate of carbonaceous species as side products. The carbon deposits formed on the surface of active sites are often considered to be the reason for deactivation rather than the aggregation of copper nanoparticles, especially at mild conditions.[6,43,61,62] However, unlike oxide-supported copper-based catalysts, the copper nanoparticles in this catalytic system are coated/embedded with/in a carbonaceous porous layer, which makes it very challenging to determine the amount of carbon deposits formed during the reaction.

In summary, even though a change in pyrolysis temperature does not change the crystallite size of the copper nanoparticles significantly, it indirectly influences the electronic environment over the active Cu sites through modification of the defect site density on the carbonaceous layer covering these sites. And this influence on the electronic environment of the active sites leads to a significant variation in the measures of catalytic performance: activity, product selectivity, and stability. These results demonstrate that CuBTC offers an excellent platform for the development of carbon-embedded copper catalysts, for which the catalytic properties can be tuned by the choice of the pyrolysis temperature depending on the specific needs of the target reaction.

4. CONCLUSIONS

Here, we synthesized a family of carbon-embedded copper catalysts by pyrolyzing CuBTC at different temperatures. Characterization data illustrated that the agglomerates of copper nanoparticles embedded in carbon were formed during pyrolysis and that the corresponding surface properties can be tuned by the choice of pyrolysis temperature. The defect density on carbon is enhanced with an increase in the pyrolysis temperature, evident from an increase in the I_D/I_G ratio observed in the Raman spectra of the corresponding samples. The XPS data, on the other hand, indicated that this increase in defect density on the surface leads to an increase in the electron density on the active copper centers. The catalysts were tested for partial hydrogenation of 1,3-butadiene to probe the consequences of these variations in surface properties at 130 °C and atmospheric pressure. Results showed that each CuBTC-derived catalyst provides a partial hydrogenation selectivity of above 98%. The catalyst prepared by pyrolysis at 900 °C, Cu@C-900, showed a stable performance for more than 12 h, while the other samples prepared at lower pyrolysis temperatures showed deactivation during the same TOS period. The data also illustrated a strong dependency of the initial TOF values on the defect sites of carbon, which can be tuned by the choice of pyrolysis temperature. These results present a versatile approach to prepare carbon-embedded copper catalysts with tunable catalytic properties.

■ ASSOCIATED CONTENT

Supporting Information

The Supporting Information is available free of charge at https://pubs.acs.org/doi/10.1021/acs.iecr.1c04741.

Additional results on catalyst characterization (PDF)

■ AUTHOR INFORMATION

Corresponding Author

Alper Uzun − *Department of Chemical and Biological Engineering, Koç University TÜPRAŞ Energy Center (KUTEM), and Koç University Surface Science and Technology Center (KUYTAM), Koç University, 34450*

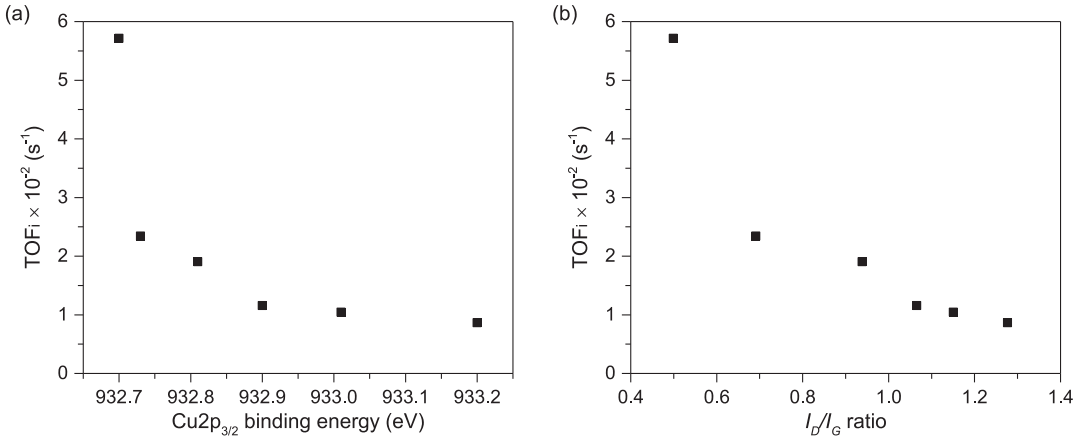


Figure 10. Initial TOF_i values as a function of (a) Cu $2p_{3/2}$ binding energy (eV) and (b) I_D/I_G ratio. TOF_i values are in s^{-1} (given as (mol of 1,3-butadiene converted) × (mol of exposed Cu × s)$^{-1}$), where the moles of exposed copper sites were determined by N_2O chemisorption and H_2 pulse reduction measurements.

https://doi.org/10.1021/acs.iecr.1c04741
Ind. Eng. Chem. Res. 2022, 61, 2068−2080

Istanbul, Turkey; orcid.org/0000-0001-7024-2900; Phone: +90 (212) 338-1754; Email: auzun@ku.edu.tr

Authors

Ahsan Jalal − *Department of Chemical and Biological Engineering and Koç University TÜPRAŞ Energy Center (KUTEM), Koç University, 34450 Istanbul, Turkey*

Yuxin Zhao − *Department of Chemical and Biological Engineering and Koç University TÜPRAŞ Energy Center (KUTEM), Koç University, 34450 Istanbul, Turkey;* orcid.org/0000-0001-5133-1940

Complete contact information is available at: https://pubs.acs.org/10.1021/acs.iecr.1c04741

Author Contributions

‖A.J. and Y.Z. contributed equally.

Notes

The authors declare no competing financial interest.

■ ACKNOWLEDGMENTS

This study is supported by Koç University TÜPRAŞ Energy Center (KUTEM). A.J. acknowledges a HEC-Pakistan scholarship. Y.Z. acknowledges a Fung Scholarship. We thank Dr. Uğur Ünal, Dr. Barış Yağcı, Gülsu Şimşek, and Amir Motallebzadeh of Koç University Surface Science and Technology Center (KUYTAM) for providing help with TEM, SEM, Raman spectroscopy, and BET measurements. A.U. acknowledges the METU Prof. Dr. Mustafa N. Parlar Education and Research Foundation's 2019 Research Incentive Award.

■ REFERENCES

(1) Bruno, J. E.; Dwarica, N. S.; Whittaker, T. N.; Hand, E. R.; Guzman, C. S., IV; Dasgupta, A.; Chen, Z.; Rioux, R. M.; Chandler, B. D. Supported Ni−Au Colloid Precursors for Active, Selective, and Stable Alkyne Partial Hydrogenation Catalysts. *ACS Catal.* **2020**, *10* (4), 2565−2580.

(2) Jalal, A.; Uzun, A. An Exceptional Selectivity for Partial Hydrogenation on a Supported Nickel Catalyst Coated with [BMIM][BF_4]. *J. Catal.* **2017**, *350*, 86−96.

(3) Jalal, A.; Uzun, A. An Ordinary Nickel Catalyst Becomes Completely Selective for Partial Hydrogenation of 1,3-Butadiene when Coated with Tributyl(Methyl)Phosphonium Methyl Sulfate. *Appl. Catal., A* **2018**, *562*, 321−326.

(4) Lucci, F. R.; Liu, J.; Marcinkowski, M. D.; Yang, M.; Allard, L. F.; Flytzani-Stephanopoulos, M.; Sykes, E. C. H. Selective Hydrogenation of 1,3-Butadiene on Platinum−Copper Alloys at the Single-Atom Limit. *Nat. Commun.* **2015**, *6* (1), 1−8.

(5) Babucci, M.; Fang, C. Y.; Perez-Aguilar, J. E.; Hoffman, A. S.; Boubnov, A.; Guan, E.; Bare, S. R.; Gates, B. C.; Uzun, A. Controlling Catalytic Activity and Selectivity for Partial Hydrogenation by Tuning the Environment around Active Sites in Iridium Complexes Bonded to Supports. *Chem. Sci.* **2019**, *10* (9), 2623−2632.

(6) Wang, Z.; Wang, G.; Louis, C.; Delannoy, L. Novel Non-Noble Bimetallic Cu-Zn/TiO_2 Catalysts for Selective Hydrogenation of Butadiene. *J. Catal.* **2017**, *347*, 185−196.

(7) Aguilar-Tapia, A.; Delannoy, L.; Louis, C.; Han, C. W.; Ortalan, V.; Zanella, R. Selective Hydrogenation of 1,3-Butadiene over Bimetallic Au-Ni/TiO_2 Catalysts Prepared by Deposition-Precipitation with Urea. *J. Catal.* **2016**, *344*, 515−523.

(8) Katano, S.; Kato, H. S.; Kawai, M.; Domen, K. Partial Hydrogenation of 1,3-Butadiene on Hydrogen-Precovered Pd (110) in the Balance of π-Bonded C_4 Hydrocarbon Reactions. *J. Phys. Chem. C* **2008**, *112* (44), 17219−17224.

(9) Zhang, X.; Shi, H.; Xu, B. Catalysis by Gold: Isolated Surface Au^{3+} Ions Are Active Sites for Selective Hydrogenation of 1,3-butadiene over Au/ZrO_2 Catalysts. *Angew. Chem., Int. Ed.* **2005**, *117* (43), 7294−7297.

(10) Hugon, A.; Delannoy, L.; Louis, C. Supported Gold Catalysts for Selective Hydrogenation of 1,3-Butadiene in the Presence of an Excess of Alkenes. *Gold Bull.* **2008**, *41* (2), 127−138.

(11) Hugon, A.; Delannoy, L.; Krafft, J.-M.; Louis, C. Selective Hydrogenation of 1,3-Butadiene in the Presence of an Excess of Alkenes over Supported Bimetallic Gold−Palladium Catalysts. *J. Phys. Chem. C* **2010**, *114* (24), 10823−10835.

(12) Hou, R.; Yu, W.; Porosoff, M. D.; Chen, J. G.; Wang, T. Selective Hydrogenation of 1,3-Butadiene on PdNi Bimetallic Catalyst: From Model Surfaces to Supported Catalysts. *J. Catal.* **2014**, *316*, 1−10.

(13) Yan, H.; Cheng, H.; Yi, H.; Lin, Y.; Yao, T.; Wang, C.; Li, J.; Wei, S.; Lu, J. Single-Atom Pd_1/Graphene Catalyst Achieved by Atomic Layer Deposition: Remarkable Performance in Selective Hydrogenation of 1,3-Butadiene. *J. Am. Chem. Soc.* **2015**, *137* (33), 10484−10487.

(14) Huang, X.; Xia, Y.; Cao, Y.; Zheng, X.; Pan, H.; Zhu, J.; Ma, C.; Wang, H.; Li, J.; You, R. Enhancing Both Selectivity and Coking-Resistance of a Single-Atom Pd_1/C_3N_4 Catalyst for Acetylene Hydrogenation. *Nano Res.* **2017**, *10* (4), 1302−1312.

(15) Huang, X.; Yan, H.; Huang, L.; Zhang, X.; Lin, Y.; Li, J.; Xia, Y.; Ma, Y.; Sun, Z.; Wei, S. Toward Understanding of the Support Effect on Pd_1 Single-Atom-Catalyzed Hydrogenation Reactions. *J. Phys. Chem. C* **2018**, *123* (13), 7922−7930.

(16) Feng, Y.; Zhou, L.; Wan, Q.; Lin, S.; Guo, H. Selective Hydrogenation of 1,3-Butadiene Catalyzed by a Single Pd Atom Anchored on Graphene: The Importance of Dynamics. *Chem. Sci.* **2018**, *9* (27), 5890−5896.

(17) Konsolakis, M.; Lykaki, M. Recent Advances on the Rational Design of Non-Precious Metal Oxide Catalysts Exemplified by CuO_x/CeO_2 Binary System: Implications of Size, Shape and Electronic Effects on Intrinsic Reactivity and Metal-Support Interactions. *Catalysts* **2020**, *10* (2), 160.

(18) Wezendonk, T. A.; Santos, V. P.; Nasalevich, M. A.; Warringa, Q. S. E.; Dugulan, A. I.; Chojecki, A.; Koeken, A. C. J.; Ruitenbeek, M.; Meima, G.; Islam, H.-U. Elucidating the Nature of Fe Species during Pyrolysis of the Fe-BTC MOF into Highly Active and Stable Fischer−Tropsch Catalysts. *ACS Catal.* **2016**, *6* (5), 3236−3247.

(19) Luo, Q.-X.; Guo, L.-P.; Yao, S.-Y.; Bao, J.; Liu, Z.-T.; Liu, Z.-W. Cobalt Nanoparticles Confined in Carbon Matrix for Probing the Size Dependence in Fischer−Tropsch Synthesis. *J. Catal.* **2019**, *369*, 143−156.

(20) Zhang, Z.; Liu, C.; Liu, D.; Shang, Y.; Yin, X.; Zhang, P.; Mamba, B. B.; Kuvarega, A. T.; Gui, J. Hydrothermal Carbon-Supported Ni Catalysts for Selective Hydrogenation of 5-Hydroxymethylfurfural toward Tunable Products. *J. Mater. Sci.* **2020**, *55* (29), 14179−14196.

(21) Santos, V. P.; Wezendonk, T. A.; Jaén, J. J. D.; Dugulan, A. I.; Nasalevich, M. A.; Islam, H.-U.; Chojecki, A.; Sartipi, S.; Sun, X.; Hakeem, A. A. Metal Organic Framework-Mediated Synthesis of Highly Active and Stable Fischer−Tropsch Catalysts. *Nat. Commun.* **2015**, *6* (1), 6451.

(22) Ceatră, L.; Pârvulescu, O. C.; Rodríguez Ramos, I.; Dobre, T. Preparation, Characterization, and Testing of a Carbon-Supported Catalyst Obtained by Slow Pyrolysis of Nickel Salt Impregnated Vegetal Material. *Ind. Eng. Chem. Res.* **2016**, *55* (6), 1491−1502.

(23) Fortea-Pérez, F. R.; Mon, M.; Ferrando-Soria, J.; Boronat, M.; Leyva-Pérez, A.; Corma, A.; Herrera, J. M.; Osadchii, D.; Gascon, J.; Armentano, D.; Pardo, E. The MOF-Driven Synthesis of Supported Palladium Clusters with Catalytic Activity for Carbene-Mediated Chemistry. *Nat. Mater.* **2017**, *16* (7), 760−766.

(24) Dupuis, A.-C. The Catalyst in the CCVD of Carbon Nanotubes—a Review. *Prog. Mater. Sci.* **2005**, *50* (8), 929−961.

(25) Jüntgen, H. Activated Carbon as Catalyst Support: A Review of New Research Results. *Fuel* **1986**, *65* (10), 1436−1446.

(26) Nakatsuka, K.; Yoshii, T.; Kuwahara, Y.; Mori, K.; Yamashita, H. Controlled Pyrolysis of Ni-MOF-74 as a Promising Precursor for the Creation of Highly Active Ni Nanocatalysts in Size-Selective Hydrogenation. *Chem.—Eur. J.* **2018**, *24* (4), 898−905.
(27) Akarçay, Ö.; Kurtoğlu, S. F.; Uzun, A. Ammonia Decomposition on a Highly-Dispersed Carbon-Embedded Iron Catalyst Derived from Fe-BTC: Stable and High Performance at Relatively Low Temperatures. *Int. J. Hydrogen Energy* **2020**, *45* (53), 28664−28681.
(28) Odoom-Wubah, T.; Li, Q.; Chen, M.; Fang, H.; Asare Bediako, B. B.; Adilov, I.; Huang, J.; Li, Q. Influence of Preparation Methods on the Catalytic Activity of Pd−Cu/Mn_2O_3 Catalyst in the Hydrogenation of 1,3-Butadiene. *ACS omega* **2019**, *4* (1), 1300−1310.
(29) Wehrli, J. T.; Thomas, D. J.; Wainwright, M. S.; Trimm, D. L.; Cant, N. W. Selective Hydrogenation of Propyne over Supported Copper Catalysts: Influence of Support. *Appl. Catal.* **1991**, *70* (1), 253−262.
(30) Bridier, B.; López, N.; Pérez-Ramírez, J. Partial Hydrogenation of Propyne over Copper-Based Catalysts and Comparison with Nickel-Based Analogues. *J. Catal.* **2010**, *269* (1), 80−92.
(31) Chui, S. S.-Y.; Lo, S. M.-F.; Charmant, J. P. H.; Orpen, A. G.; Williams, I. D. A Chemically Functionalizable Nanoporous Material $[Cu_3(TMA)_2(H_2O)_3]$n. *Science* **1999**, *283* (5405), 1148−1150.
(32) Li, J.; Zhou, N.; Song, J.; Fu, L.; Yan, J.; Tang, Y.; Wang, H. Cu−MOF-Derived Cu/Cu_2O Nanoparticles and CuN_xC_y Species to Boost Oxygen Reduction Activity of Ketjenblack Carbon in Al−Air Battery. *ACS Sustainable Chem. Eng.* **2018**, *6* (1), 413−421.
(33) Zhang, S.; Liu, H.; Sun, C.; Liu, P.; Li, L.; Yang, Z.; Feng, X.; Huo, F.; Lu, X. CuO/Cu_2O Porous Composites: Shape and Composition Controllable Fabrication Inherited from Metal Organic Frameworks and Further Application in CO Oxidation. *J. Mater. Chem. A* **2015**, *3* (10), 5294−5298.
(34) Niu, H.; Liu, S.; Cai, Y.; Wu, F.; Zhao, X. MOF Derived Porous Carbon Supported Cu/Cu_2O Composite as High Performance Non-Noble Catalyst. *Micropor. Mesopor. Mater.* **2016**, *219*, 48−53.
(35) Zhao, Y.; Wu, X.; Zhou, J.; Wang, Y.; Wang, S.; Ma, X. MOF-Derived Cu@C Catalyst for the Liquid-Phase Hydrogenation of Esters. *Chem. Lett.* **2018**, *47* (7), 883−886.
(36) Bak, W.; Kim, H. S.; Chun, H.; Yoo, W. C. Facile Synthesis of Metal/Metal Oxide Nanoparticles inside a Nanoporous Carbon Matrix (M/MO@C) through the Morphology-Preserved Transformation of Metal−Organic Framework. *Chem. Commun.* **2015**, *51* (33), 7238−7241.
(37) Gong, Q.; Sun, L.; Wu, Z.; Huo, L.; Zhao, H. Enhanced Non-Enzymatic Glucose Sensing of Cu−BTC-Derived Porous Copper@Carbon Agglomerate. *J. Mater. Sci.* **2018**, *53* (10), 7305−7315.
(38) Wei, C.; Li, X.; Xu, F.; Tan, H.; Li, Z.; Sun, L.; Song, Y. Metal Organic Framework-Derived Anthill-like Cu@ Carbon Nanocomposites for Nonenzymatic Glucose Sensor. *Anal. Methods* **2014**, *6* (5), 1550−1557.
(39) Raoof, J.-B.; Hosseini, S. R.; Ojani, R.; Mandegarzad, S. MOF-Derived Cu/Nanoporous Carbon Composite and Its Application for Electro-Catalysis of Hydrogen Evolution Reaction. *Energy* **2015**, *90*, 1075−1081.
(40) Das, R.; Pachfule, P.; Banerjee, R.; Poddar, P. Metal and Metal Oxide Nanoparticle Synthesis from Metal Organic Frameworks (MOFs): Finding the Border of Metal and Metal Oxides. *Nanoscale* **2012**, *4* (2), 591−599.
(41) Zeeshan, M.; Nozari, V.; Keskin, S.; Uzun, A. Structural Factors Determining Thermal Stability Limits of Ionic Liquid/MOF Composites: Imidazolium Ionic Liquids Combined with CuBTC and ZIF-8. *Ind. Eng. Chem. Res.* **2019**, *58* (31), 14124−14138.
(42) Kurtoğlu, S. F.; Soyer-Uzun, S.; Uzun, A. Modifying the Structure of Red Mud by Simple Treatments for High and Stable Performance in CO_x-Free Hydrogen Production from Ammonia. *Int. J. Hydrogen Energy* **2018**, *43* (45), 20525−20537.
(43) Zhao, Y.; Jalal, A.; Uzun, A. Interplay between Copper Nanoparticle Size and Oxygen Vacancy on Mg-Doped Ceria Controls Partial Hydrogenation Performance and Stability. *ACS Catal.* **2021**, *11*, 8116−8131.
(44) Al-Janabi, N.; Hill, P.; Torrente-Murciano, L.; Garforth, A.; Gorgojo, P.; Siperstein, F.; Fan, X. Mapping the Cu-BTC Metal−Organic Framework (HKUST-1) Stability Envelope in the Presence of Water Vapour for CO_2 Adsorption from Flue Gases. *Chem. Eng. J.* **2015**, *281*, 669−677.
(45) Sezginel, K. B.; Keskin, S.; Uzun, A. Tuning the Gas Separation Performance of CuBTC by Ionic Liquid Incorporation. *Langmuir* **2016**, *32* (4), 1139−1147.
(46) An, B.; Cheng, K.; Wang, C.; Wang, Y.; Lin, W. Pyrolysis of Metal−Organic Frameworks to Fe_3O_4@Fe_5C_2 Core−Shell Nanoparticles for Fischer−Tropsch Synthesis. *ACS Catal.* **2016**, *6* (6), 3610−3618.
(47) Beyazay, T.; Oztuna, F. E. S.; Unal, O.; Acar, H. Y.; Unal, U. Free-Standing N-doped Reduced Graphene Oxide Papers Decorated with Iron Oxide Nanoparticles: Stable Supercapacitor Electrodes. *ChemElectroChem* **2019**, *6* (14), 3774−3781.
(48) Guizani, C.; Haddad, K.; Limousy, L.; Jeguirim, M. New Insights on the Structural Evolution of Biomass Char upon Pyrolysis as Revealed by the Raman Spectroscopy and Elemental Analysis. *Carbon* **2017**, *119*, 519−521.
(49) Ferrari, A. C.; Robertson, J. Interpretation of Raman Spectra of Disordered and Amorphous Carbon. *Phys. Rev. B* **2000**, *61* (20), 14095.
(50) Ferrari, A. C.; Robertson, J. Raman Spectroscopy of Amorphous, Nanostructured, Diamond-like Carbon, and Nanodiamond. *Philos. Trans. Royal Soc. A* **2004**, *362* (1824), 2477−2512.
(51) Cheng, J.; Xuan, X.; Yang, X.; Zhou, J.; Cen, K. Selective Reduction of CO_2 to Alcohol Products on Octahedral Catalyst of Carbonized Cu(BTC) Doped with Pd Nanoparticles in a Photoelectrochemical Cell. *Chem. Eng. J.* **2019**, *358*, 860−868.
(52) Weng, Y.; Guan, S.; Wang, L.; Lu, H.; Meng, X.; Waterhouse, G. I. N.; Zhou, S. Defective Porous Carbon Polyhedra Decorated with Copper Nanoparticles for Enhanced NIR-Driven Photothermal Cancer Therapy. *Small* **2020**, *16* (1), 1905184.
(53) Endo, M.; Nishimura, K.; Kim, Y. A.; Hakamada, K.; Matushita, T.; Dresselhaus, M. S.; Dresselhaus, G. Raman Spectroscopic Characterization of Submicron Vapor-Grown Carbon Fibers and Carbon Nanofibers Obtained by Pyrolyzing Hydrocarbons. *J. Mater. Res.* **1999**, *14* (12), 4474−4477.
(54) Campos-Delgado, J.; Kim, Y. A.; Hayashi, T.; Morelos-Gómez, A.; Hofmann, M.; Muramatsu, H.; Endo, M.; Terrones, H.; Shull, R. D.; Dresselhaus, M. S.; Terrones, M. Thermal Stability Studies of CVD-Grown Graphene Nanoribbons: Defect Annealing and Loop Formation. *Chem. Phys. Lett.* **2009**, *469* (1−3), 177−182.
(55) Abdel-Mageed, A. M.; Rungtaweevoranit, B.; Parlinska-Wojtan, M.; Pei, X.; Yaghi, O. M.; Behm, R. J. Highly Active and Stable Single-Atom Cu Catalysts Supported by a Metal-Organic Framework. *J. Am. Chem. Soc.* **2019**, *141* (13), 5201−5210.
(56) Xiong, X.; You, C.; Liu, Z.; Asiri, A. M.; Sun, X. Co-Doped CuO Nanoarray: An Efficient Oxygen Evolution Reaction Electrocatalyst with Enhanced Activity. *ACS Sustainable Chem. Eng.* **2018**, *6* (3), 2883−2887.
(57) Harilal, M.; Krishnan, S. G.; Pal, B.; Reddy, M. V.; Ab Rahim, M. H.; Yusoff, M. M.; Jose, R. Environment-Modulated Crystallization of Cu_2O and CuO Nanowires by Electrospinning and Their Charge Storage Properties. *Langmuir* **2018**, *34* (5), 1873−1882.
(58) Nieminen, V.; Kumar, N.; Datka, J.; Päivärinta, J.; Hotokka, M.; Laine, E.; Salmi, T.; Murzin, D. Y. Active Copper Species in 1-Butene Skeletal Isomerization: Comparison between Copper-Modified MCM-41 and Beta Catalysts. *Micropor. Mesopor. Mater.* **2003**, *60* (1−3), 159−171.
(59) Dimitrov, C.; Leach, H. F. Studies of N-Butene Isomerization over Sodium X Zeolite and Copper X Zeolite. *J. Catal.* **1969**, *14* (4), 336−347.
(60) Gómez, G.; Belelli, P. G.; Cabeza, G. F.; Castellani, N. J. A Theoretical View of 1,3-Butadiene Selective Hydrogenation toward

https://doi.org/10.1021/acs.iecr.1c04741
Ind. Eng. Chem. Res. 2022, 61, 2068−2080

Cis-2-Butene on PdNi Layered Catalyst. *Appl. Surf. Sci.* **2015**, *353*, 820−828.
(61) Shi, X.; Lin, Y.; Huang, L.; Sun, Z.; Yang, Y.; Zhou, X.; Vovk, E.; Liu, X.; Huang, X.; Sun, M.; Wei, S.; Lu, J. Copper Catalysts in Semi-Hydrogenation of Acetylene: From Single Atoms to Nanoparticles. *ACS Catal.* **2020**, *10*, 3495.
(62) Nishimura, E.; Inoue, Y.; Yasumori, I. The Mechanism of the Selective Hydrogenation of 1,3-Butadiene on Copper Surfaces. *Bull. Chem. Soc. Jpn.* **1975**, *48* (3), 803−807.

https://doi.org/10.1021/acs.iecr.1c04741
Ind. Eng. Chem. Res. 2022, 61, 2068−2080